Dynamic Humanoid Arm-Swing Motion via Trajectory Optimization Leveraging Speed–Torque Mode Switching of a Variable Chain Motor

Hiromi Tada[1], Takuma Hiraoka[1], Jin Hirai[1], Kunio Kojima[1], and Kei Okada[1]

***Abstract*— Achieving high athletic performance in humanoid robots requires both high joint speed and high joint torque. While transmission mechanisms have been proposed to enlarge the output envelope by varying the speed–torque characteristics, such mechanisms are disadvantageous for humanoids in terms of weight and size. Moreover, planning methods for generating dynamic humanoid motions that account for output-characteristic switching—which leads to discontinuous changes in the admissible speed–torque constraints—remain underexplored. This paper proposes a method for generating dynamic humanoid motions that exploit mode switching through trajectory optimization, using a Variable Chain Motor (VC motor) that can switch among modes with different speed–torque characteristics via an electrical circuit. Specifically, we impose the union of feasible speed–torque ranges across multiple modes as constraints on joint velocity and torque in the trajectory optimization problem. During execution on the real robot, we determine the mode at each time step based on the speed–torque profile of the optimized trajectory, enabling dynamic mode switching. We generate a dynamic arm-swing motion that maximizes forward end-effector velocity for a humanoid equipped with a VC motor at the elbow joint and validate it via real-robot experiments. We demonstrate the effectiveness of the proposed method by comparing it against fixed-output-characteristic cases, in which the actuator is used as a conventional motor.**

I. Introduction

For humanoid robots, achieving both strength and speed remains a major challenge. In brushless DC (BLDC) motors, which are the most widely used actuators in humanoids, speed and torque are proportional to back electromotive force and current, respectively; therefore, achieving both high speed and high torque requires high voltage and high current. To address this issue, the speed–torque envelope can be expanded by varying the speed–torque characteristics, and several studies have proposed introducing mechanical transmissions into robots. However, for humanoids, the increases in weight and size caused by such complex mechanisms diminish the benefits of the expanded output envelope. In addition, motion planning for humanoids has not considered how to handle speed–torque constraints that change discontinuously due to switching of output characteristics.

In this paper, we propose a trajectory-optimization-based method for generating dynamic humanoid motions using a VC motor (Variable Chain Motor) [1], which can electrically switch among multiple modes, including high-torque, intermediate, and high-speed modes. The VC motor can switch its output characteristics by changing its winding connection via a compact and lightweight electrical circuit. By imposing the union of the feasible speed–torque ranges across modes as joint velocity and torque constraints in the trajectory optimization problem, the proposed method achieves both high speed and high torque by exploiting mode switching. The timing of mode switching is then determined from the joint velocity and torque at each time step along the obtained optimal trajectory.

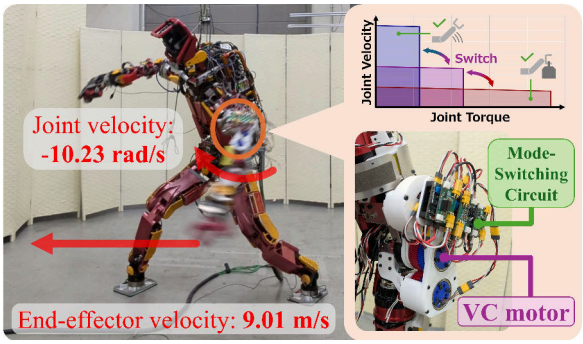


Fig. 1: A dynamic arm-swing motion that maximizes the forward end-effector velocity of a humanoid whose elbow joint is equipped with a VC motor. By exploiting speed–torque mode switching, the motion achieves both high torque and high speed.

To validate the effectiveness of the proposed method, we generate a dynamic arm-swing motion that maximizes the forward end-effector velocity of a humanoid whose elbow joint is equipped with a VC motor, and conduct real-robot experiments (Fig. 1). As a result, the proposed method achieves faster motion than a conventional motor with fixed output characteristics.

The contributions of this paper are as follows.

- We propose a motion planning method that computes a humanoid trajectory for motions involving joints with variable output characteristics under discontinuously changing speed–torque constraints and determines the switching times.
- We demonstrate through real-robot experiments that the variable output characteristics of the VC motor improve the dynamic performance of humanoid motions.

The remainder of this paper is organized as follows. Section II reviews related work. Section III formulates the speed–torque characteristics of the VC motor and describes a trajectory optimization method for generating dynamic motions with mode switching. Section IV evaluates the generated arm-swing motions and presents real-robot experimental results using the proposed method. Finally, Section V concludes the paper.

[1]The authors are with the Graduate School of Information Science and Technology, The University of Tokyo, 7-3-1 Hongo, Bunkyo-ku, Tokyo 113-8656, Japan [h-tada, t-hiraoka, hirai, k-kojima, k-okada]@jsk.imi.i.u-tokyo.ac.jp

II. Related Work

Covering a wide speed–torque range with fixed gearing typically requires either using a large and inefficient motor or imposing stringent requirements on the power supply configuration. To address this issue, a variable transmission mechanism that shifts among three gear sets with different speed ratios has been proposed [2]. Another example is the Dual-Speed Dual-Motor (DSDM) actuator [3]. However, the former involves power interruption during shifting, and although the latter enables seamless shifting, it still requires tens of milliseconds to actuate the shift brake, making it unsuitable for dynamic motions. The application of CVTs (Continuously Variable Transmissions), originally developed for vehicles, to robots has also been explored [4], and combining a CVT with series-elastic actuation has been shown to improve the performance of a jumping robot [5]. Nevertheless, the increased weight and size due to these complex mechanisms remain a major obstacle to integration in humanoids.

Meanwhile, methods that vary the speed–torque characteristics by electrically reconfiguring motor windings have been developed for automotive and air-conditioning applications [6], [7]. Compared with mechanical transmissions, this approach not only enables a more compact and lightweight design but also achieves sufficiently fast mode switching during operation [8], making it promising for dynamic humanoid motions as well. The VC motor [1] performs winding reconfiguration among multiple motors with identical windings. It is a robot-specific actuator designed to meet the strict spatial constraints of humanoids and legged robots, allowing flexible placement of multiple small motors as an alternative to a single large motor.

To realize robot motions under discontinuously changing speed–torque constraints, Girard et al., who proposed the DSDM actuator, also devised a trajectory-tracking controller that performs discrete mode selection for a single-axis system and a 3-DoF robot arm [9], [10]. Although such studies have clarified the advantages of applying variable output characteristics to robots, methods that leverage variable output characteristics to generate dynamic humanoid motions have received limited attention. We focus on combining variable output characteristics with trajectory optimization, which has been demonstrated to be effective for humanoid behaviors such as running [11] and jumping [12]. By imposing the union of the speed–torque ranges across modes as constraints, we propose a trajectory planning method for humanoids that exploits variable output characteristics within a nonconvex optimization framework [13].

III. Trajectory Optimization with Output-Characteristic Switching

A. Speed–Torque Characteristics of the VC Motor

The VC motor has a structure in which multiple units, called MCs (Motor Cells), each consisting of a small-diameter motor with custom modifications, are connected in a chain [1]. The VC motor considered in this paper, which consists of four MCs, can operate in three modes: Mode A (high torque), Mode B (intermediate), and Mode C (high speed) (with more MCs, additional modes are possible). Given upper limits on the voltage and current supplied to the VC motor, the feasible speed–torque range in each mode is shown in Fig. 3.

The change in output characteristics arises from changes in the current path caused by switching the winding connection (series or parallel) inside the VC motor (Fig. 2). Here, let I denote the current supplied to the VC motor by the motor drive circuit. In the high-torque Mode A, the windings of all four MCs are connected in series, and the current I flows through each MC. In the intermediate Mode B, two pairs of series-connected windings are connected in parallel, and the current is equally split such that $I/2$ flows through each branch. In the high-speed Mode C, all four windings are connected in parallel, and the current is divided equally so that $I/4$ flows through each MC.

The torque constants (the ratio of output torque to input current) in each mode, $K_\tau^{\mathrm{A}}, K_\tau^{\mathrm{B}}, K_\tau^{\mathrm{C}}$, can be derived by computing the total output torque of the four MCs from the current flowing through each MC and dividing the result by the input current I. Therefore, using the torque constant of a single MC, K_τ^{cell}, they are given by (1), indicating that the torque characteristic increases from Mode C to Mode A, which corresponds to having a larger number of series-connected windings. Given the maximum allowable input current $I^{\max}$, the maximum torques in each mode, $\tau^{\max,\mathrm{A}}, \tau^{\max,\mathrm{B}}, \tau^{\max,\mathrm{C}}$, can also be obtained by multiplying the corresponding torque constants by $I^{\max}$.

$$\begin{aligned} K_\tau^{\mathrm{A}} &= 4(K_\tau^{\text{cell}} I) \quad /I = 4K_\tau^{\text{cell}}, \quad \tau^{\max,\mathrm{A}} = 4K_\tau^{\text{cell}} I^{\max} \\ K_\tau^{\mathrm{B}} &= 4(K_\tau^{\text{cell}} I/2)/I = 2K_\tau^{\text{cell}}, \quad \tau^{\max,\mathrm{B}} = 2K_\tau^{\text{cell}} I^{\max} \\ K_\tau^{\mathrm{C}} &= 4(K_\tau^{\text{cell}} I/4)/I = \ K_\tau^{\text{cell}}, \quad \tau^{\max,\mathrm{C}} = \ K_\tau^{\text{cell}} I^{\max} \end{aligned} \tag{1}$$

The speed constant, defined as the ratio of rotational speed to back electromotive force, is inversely proportional to the torque constant. The speed constants in each mode, $K_v^{\mathrm{A}}, K_v^{\mathrm{B}}, K_v^{\mathrm{C}}$, expressed in terms of the speed constant of a single MC, K_v^{cell}, are given as follows, indicating that the speed characteristic increases from Mode A to Mode C. Given the maximum applicable voltage $V^{\max}$, the maximum no-load speeds in each mode, $v^{\max,\mathrm{A}}, v^{\max,\mathrm{B}}, v^{\max,\mathrm{C}}$, can also be obtained by multiplying the corresponding speed constants by $V^{\max}$.

$$\begin{aligned} K_v^{\mathrm{A}} &= K_v^{\text{cell}}/4, \quad v^{\max,\mathrm{A}} = K_v^{\text{cell}} V^{\max}/4 \\ K_v^{\mathrm{B}} &= K_v^{\text{cell}}/2, \quad v^{\max,\mathrm{B}} = K_v^{\text{cell}} V^{\max}/2 \\ K_v^{\mathrm{C}} &= K_v^{\text{cell}} \quad , \quad v^{\max,\mathrm{C}} = K_v^{\text{cell}} V^{\max} \end{aligned} \tag{2}$$

When a load torque is present, the maximum speed decreases linearly with respect to torque and becomes smaller than the value in (2); however, the rate of decrease is the same for all modes. Let the maximum speed under a load torque τ be denoted by $v^{\lim}(\tau)$ as a function of τ. For a BLDC motor with winding resistance R and speed constant K_v, when a current I is applied, the following circuit equation holds. Note that we consider the q-axis equation

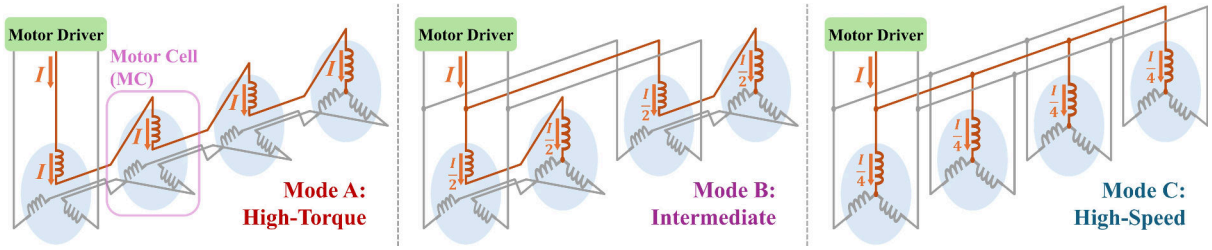


Fig. 2: Winding configurations of the VC motor for each mode. In Mode A, all four windings are connected in series. In Mode B, two series-connected windings are arranged in parallel as two identical branches. In Mode C, all four windings are connected in parallel. A larger number of series-connected windings results in a higher-torque, lower-speed characteristic.

while neglecting the cross-coupling term between the d and q axes.

$$V^{\max} = RI + \frac{v^{\lim}(\tau)}{K_v} \tag{3}$$

In addition, the following relations hold for the no-load maximum speed $v^{\max}$ and the torque constant K_τ. Note that $\sqrt{3}$ is the factor used to convert the speed constant expressed with the peak line-to-line voltage into the torque constant expressed with the peak phase current.

$$v^{\max} = K_v V^{\max}, \quad \tau = K_\tau I, \quad K_\tau K_v = \sqrt{3} \tag{4}$$

From (3) and (4), we obtain the following. Here, α is the inverse of the rate at which the maximum speed $v^{\lim}(\tau)$ decreases with respect to the torque τ.

$$v^{\lim}(\tau) = v^{\max} - \frac{\tau}{\alpha}, \quad \alpha = \frac{K_\tau^2}{\sqrt{3}R} \tag{5}$$

Let the winding resistance of an MC be R^{cell}. Then, the winding resistance in Modes A, B, and C becomes $4R^{\text{cell}}$, R^{cell}, and $R^{\text{cell}}/4$, respectively. Substituting these into (5) together with the torque constants in each mode shown in (1), we obtain the following.

$$\alpha = \frac{4(K_\tau^{\text{cell}})^2}{\sqrt{3}R^{\text{cell}}} \tag{6}$$

Therefore, the rate at which the maximum speed decreases with respect to torque is determined solely by the winding resistance and torque constant of the MC, and does not depend on the mode.

By substituting the no-load maximum speed of each mode shown in (2) into (5), we obtain the corresponding speed limit as a function of torque. Together with the torque limit of each mode shown in (1), these limits yield the speed–torque ranges of the VC motor shown in Fig. 3.

B. Formulation of Speed–Torque Constraints Considering VC Motor Mode Switching

Robot motion planning is performed under constraints on joint velocity and torque so that the resulting motion can be executed within the capabilities of the real actuator. In some cases, constant upper bounds are imposed on velocity and torque independently; however, for dynamic motions that require both high speed and high torque, the reduction in the speed limit as a function of the output torque, as shown in (5), cannot be neglected. To account for this effect, it is desirable to formulate the constraint by defining the torque limit $\tau^{\lim}(v)$ as a function of the continuously varying velocity v. Accordingly, we transform (5) into the following function of v, which represents the admissible range for torque τ. Here, $\tau^{\max}$ and $v^{\max}$ denote the maximum torque and the no-load maximum speed of the joint, respectively.

$$\begin{cases} |\tau| \le \tau^{\lim}(v) = \min(\tau^{\max}, -\alpha(|v| - v^{\max})) \\ |v| \le v^{\max} \end{cases} \tag{7}$$

For the VC motor, it is necessary to represent the speed–torque range of each mode described in Section III-A. Therefore, we use the following constraint, which represents the union of the regions given by (7) over all modes without explicit mode variables. The torque limit $\tau^{\lim}(v)$ appearing in (8) corresponds to the stair-step function indicated by the orange line in Fig. 3.

$$\begin{cases} |\tau| \le \tau^{\lim}(v) = \max \begin{pmatrix} \min(\tau^{\max,\mathrm{A}}, -\alpha(|v| - v^{\max,\mathrm{A}})) \\ \min(\tau^{\max,\mathrm{B}}, -\alpha(|v| - v^{\max,\mathrm{B}})) \\ \min(\tau^{\max,\mathrm{C}}, -\alpha(|v| - v^{\max,\mathrm{C}})) \end{pmatrix} \\ |v| \le v^{\max,\mathrm{C}} \end{cases} \tag{8}$$

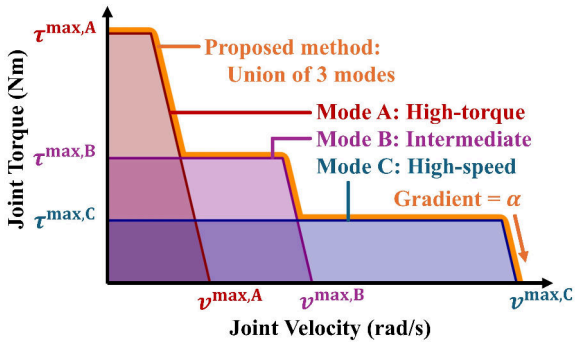


Fig. 3: Speed–torque ranges of the VC motor. The red, purple, and blue regions represent the ranges of Modes A, B, and C, respectively. The union of these ranges, indicated by the orange line, is imposed as the speed–torque constraint in trajectory optimization. For consistency with expressing the torque limit as a function of velocity in Section III-B, note that the horizontal axis represents velocity, unlike a typical speed–torque characteristic plot.

The inequality in (8) can be imposed directly. In our implementation, we use the equivalent bounded-slack form $\tau = s\tau^{\lim}(v)$, $s \in [-1, 1]$, only to represent the two-sided torque bound with a bounded variable; this implementation choice is not essential to the formulation. The constraint

in (8) represents the instantaneous feasible speed–torque envelope obtained as the union of all modes, so no discrete mode variable is required during trajectory optimization. A mixed-integer or hybrid formulation could optimize the mode sequence and switching penalties, but would introduce mode-selection integer variables for each time node of each VC motor. We therefore adopt the continuous union-constraint formulation, which is compatible with standard gradient-based humanoid trajectory optimization, and then recover the executable mode schedule from the optimized speed–torque trajectory.

During execution, at each discretized time k, with R_m denoting the range of mode m, $\mathcal{M}_k = \{m \in \{\mathrm{A}, \mathrm{B}, \mathrm{C}\} \mid (v_k, \tau_k) \in R_m\}$ is formed, and the first feasible mode in the order A, B, C is selected.

In this paper, we smoothly approximate the max and min functions in (7) and (8) using log-sum-exp (LSE) as follows, where the parameter k controls the sharpness of the approximation, and treat the problem as a continuously differentiable nonlinear optimization problem.

$$\begin{aligned} \max(x, y, z) &\approx k \ln(\exp(x/k) + \exp(y/k) + \exp(z/k)) \\ \min(x, y) &\approx -k \ln(\exp(-x/k) + \exp(-y/k)) \end{aligned} \tag{9}$$

C. Formulation of Humanoid Trajectory Optimization

In this section, we define a trajectory optimization problem for generating dynamic humanoid motions using the speed–torque constraints described in Section III-B. We integrate a VC motor into the left elbow joint of a humanoid robot [14] and generate an arm-swing motion that maximizes the forward velocity of the left-hand end-effector. The humanoid has 33 degrees of freedom excluding the fingers; however, we fix the neck and some wrist joints and treat the system as having $N^{\mathrm{DoF}} = 27$ degrees of freedom.

We pose the following trajectory optimization problem. The decision variables are the generalized coordinates $\boldsymbol{q}(t)$, generalized velocities $\boldsymbol{v}(t)$, generalized accelerations $\boldsymbol{a}(t)$, and a 12-dimensional vector $\boldsymbol{w}(t)$ that collects the forces and moments exerted on the left and right feet by the ground, for $t \in [0, t_{\mathrm{f}}]$. For the bounded-slack implementation of the two-sided torque bounds, the auxiliary vector $\boldsymbol{s}(t) \in [-1, 1]^{N^{\mathrm{DoF}}}$ is also included. We minimize the cost function f subject to equality constraints $\boldsymbol{g}$ and inequality constraints $\boldsymbol{h}$.

$$\begin{aligned} \underset{\boldsymbol{q},\boldsymbol{v},\boldsymbol{a},\boldsymbol{w},\boldsymbol{s}}{\text{minimize}} \quad & f(\boldsymbol{q}, \boldsymbol{v}, \boldsymbol{a}, \boldsymbol{w}, \boldsymbol{s}) \\ \text{subject to} \quad & \boldsymbol{g}(\boldsymbol{q}, \boldsymbol{v}, \boldsymbol{a}, \boldsymbol{w}, \boldsymbol{s}) = \boldsymbol{0} \\ & \boldsymbol{h}(\boldsymbol{q}, \boldsymbol{v}, \boldsymbol{a}, \boldsymbol{w}, \boldsymbol{s}) \leq \boldsymbol{0} \end{aligned} \tag{10}$$

The joint torque is computed as follows.

$$\boldsymbol{\tau}(t) = \boldsymbol{\tau}^{\mathrm{ID}}(\boldsymbol{q}, \boldsymbol{v}, \boldsymbol{a}, \boldsymbol{w}) + \boldsymbol{B}\boldsymbol{v}(t) + \boldsymbol{J}_{\mathrm{r}}\boldsymbol{a}(t) \tag{11}$$

Here, $\boldsymbol{\tau}^{\mathrm{ID}}$ is the inverse-dynamics torque, $\boldsymbol{B}$ and $\boldsymbol{J}_{\mathrm{r}}$ are diagonal matrices of viscous friction coefficients and rotor inertias, respectively, and $\boldsymbol{\tau}^{\mathrm{lim}}(\boldsymbol{v}(t))$ is defined by (7) and (8). We impose the corresponding velocity–torque constraint as follows. In our implementation, this constraint is represented using the bounded-slack form described in Section III-B.

$$|\boldsymbol{\tau}(t)| \leq \boldsymbol{\tau}^{\mathrm{lim}}(\boldsymbol{v}(t)) \tag{12}$$

The trajectory duration is set to $t_{\mathrm{f}} = 3.0$ s. The time discretization step size is set to 0.01 s around the mid-interval (1.2–1.8 s), where the motion is fastest, and outside this interval we use a step size that increases linearly with the step index toward the start and end times, up to a maximum of 0.11 s.

The cost function f is given by the following expression.

$$\begin{aligned} f = &- W_1 v_x^{\mathrm{EE}}(t_{\mathrm{m}}) + \sum_{i=1}^{N^{\mathrm{DoF}}} W_{2,i} \int_0^{t_{\mathrm{f}}} \left(\frac{da_i(t)}{dt} \right)^2 dt \\ &+ W_3 \int_0^{t_{\mathrm{f}}} (||\boldsymbol{w}(t)||^2 - (F_{\mathrm{R},z})^2 - (F_{\mathrm{L},z})^2) dt \end{aligned} \tag{13}$$

The first term maximizes the value of the forward left-hand end-effector velocity v_x^{EE} at the mid-time $t_{\mathrm{m}} = t_{\mathrm{f}}/2$, with weight $W_1 = 1$. The second term is a regularization term that minimizes the sum of squared joint jerks (the time derivative of the joint acceleration a_i) for joint i. The weight $W_{2,i}$ is set to 5×10^{-9} for the left elbow joint and 5×10^{-3} for all other joints. The third term minimizes the sum of squares of the horizontal components of the ground reaction forces and the three-axis moments, excluding the vertical ground reaction forces of the right and left feet, $F_{\mathrm{R},z}$ and $F_{\mathrm{L},z}$, from the foot wrench $\boldsymbol{w}$. The weight is set to $W_3 = 5 \times 10^{-5}$. This term guides the search toward solutions that better satisfy the whole-body balance constraints.

In addition to the velocity–torque constraint in (12), the equality constraints $\boldsymbol{g}$ include the following.

- The joint angles at the initial and terminal times are fixed to predetermined values.
- The joint velocities and joint accelerations at the initial and terminal times are set to zero.
- To keep the feet fixed, the velocities of the left and right foot links are set to zero.
- The height of the left-hand end-effector at the mid-time is set to 0.5 m above the ground.

The inequality constraints $\boldsymbol{h}$ include the following.

- Upper and lower limits are imposed on the joint angles.
- The horizontal components of the ground reaction force are constrained to be no greater than 0.7 times the vertical component (friction cone constraint).
- The ZMP (Zero Moment Point) computed from the ground reaction forces is constrained to lie within the support polygon of both feet (ZMP constraint).

IV. Generation and Evaluation of Dynamic Arm-Swing Motion

In this section, we generate dynamic arm-swing motions by solving the trajectory optimization problem described above, and evaluate the resulting trajectories and validate them through real-robot experiments.

For comparison with the case where the actuator is used as a conventional motor with fixed output characteristics, we generate motions under the following four conditions, which differ in the speed–torque constraints applied to the left elbow joint.

(a) The VC motor is fixed to Mode A (high torque).

(b) The VC motor is fixed to Mode B (intermediate).
(c) The VC motor is fixed to Mode C (high speed).
(d) Mode switching is allowed.

TABLE I: Joint speed–torque limits and dynamic parameters.

Joint	Speed limit (rad/s)	Torque limit (Nm)	Viscous coefficient (Nms/rad)	Rotor inertia (kg m^2)
Chest-r/p	2.17	383.8	3.07	2.06
Chest-y	2.17	191.9	3.07	1.03
Collar	1.81	230.3	3.07	1.49
Shoulder-p/r/y	1.81	230.3	3.07	1.49
Right elbow	1.81	230.3	3.07	1.49
Left elbow	Shown in Table II.		0.77	0.51
Wrist-y	1.81	230.3	3.07	1.49
Hip-y	3.47	119.9	3.07	0.40
Hip-r	2.17	191.9	3.07	1.03
Hip-p	3.47	239.9	1.20	0.81
Knee	3.47	239.9	1.20	0.81
Ankle-p	2.89	143.9	3.07	0.58
Ankle-r	3.44	120.7	3.11	0.41

TABLE II: Speed–torque limits of the left elbow joint equipped with a VC motor.

Mode	A	B	C
Speed limit (rad/s)	3.90	7.80	15.60
Torque limit (Nm)	106.6	53.3	26.7

The parameters of each joint are listed in Table I and Table II. For the maximum speed of each joint, we use the no-load speed at a peak line-to-line voltage of 24 V. We intentionally used a low system voltage to make the speed limit active and highlight the benefit of mode switching. Note that the speed limits of the other joints decrease significantly compared with higher-voltage operation; therefore, the achievable end-effector speed is smaller than in previous work using the same humanoid [13]. For the maximum torque of each joint, we use the output torque at a peak phase current of 20 A.

The value of k in (9) is set for each joint; for joint i, we set $k_i = 0.01\tau_i^{\max}$ using its maximum torque $\tau_i^{\max}$ (for the VC motor, we used the maximum torque in Mode A). Note that the velocity–torque constraint under condition (d) involves a max function, and the approximation slightly relaxes the constraint; therefore, we evaluate the degree of violation of the original velocity–torque constraint for the generated trajectories.

To solve the trajectory optimization problem, we used the mathematical optimization framework CasADi [15] and the nonlinear optimization solver Ipopt [16], which is based on a primal–dual interior-point method. For kinematics and dynamics computations, we used Pinocchio [17].

A. *Evaluation of the Optimal Trajectory*

Table III summarizes the peak forward end-effector velocity and the peak left elbow joint velocity along the optimal trajectories obtained by solving the optimization problems above. The optimal trajectory for condition (d) is shown in Fig. 4. The left elbow joint velocity for each condition is shown in Fig. 5, and the corresponding speed–torque trajectories are shown in Fig. 6.

With mode switching allowed in condition (d), the peak forward end-effector velocity increased by 7.7% and the peak left elbow joint velocity increased by 10.2% compared with condition (c), the fastest fixed-mode case. Under conditions (a) and (b), the speed limit becomes active despite the high torque capability. Under condition (c), the high-speed range is available, but the low torque limit restricts acceleration in the low-speed region. In contrast, under condition (d), the active constraint shifts from Mode A through Mode B to the

TABLE III: Peak forward end-effector velocity and left elbow joint velocity of the optimal trajectories.

Condition	(a)	(b)	(c)	(d)
Peak forward velocity of the end-effector (m/s)	6.20	8.16	8.26	8.89
Peak left elbow joint velocity (rad/s)	-3.87	-7.65	-9.13	-10.06

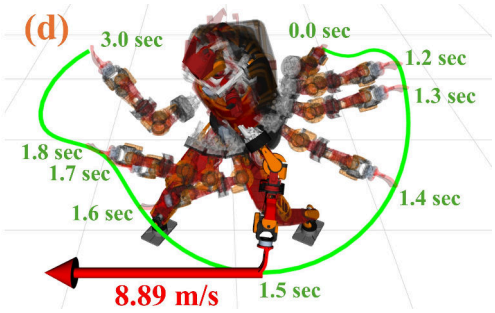


Fig. 4: Optimal trajectory under condition (d), where mode switching is allowed. The peak forward end-effector velocity reaches 8.89 m/s, 7.7% higher than condition (c); the right arm is omitted for clarity.

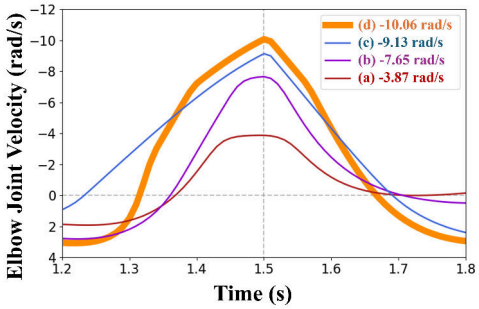


Fig. 5: Left elbow joint velocity under each condition. Condition (d) combines high acceleration and high speed, reaching -10.06 rad/s, 10.2% higher than condition (c).

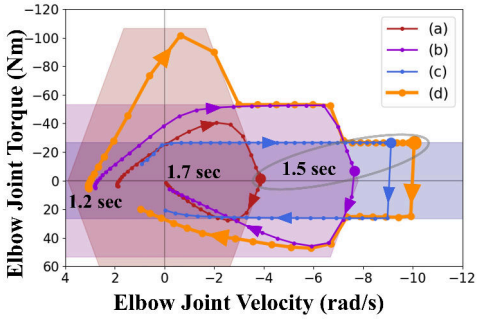


Fig. 6: Speed–torque trajectories of the left elbow joint under each condition. Condition (d) follows the higher-torque boundaries of Modes A and B at low speed and then enters the high-speed range of Mode C; colored regions show the mode ranges for all four quadrants.

high-speed Mode C as the speed increases. This trajectory therefore uses both high torque at low speed and high speed after acceleration, leading to improvements in both joint velocity and end-effector speed. These results show that the proposed method can generate dynamic humanoid arm-swing motions that include VC motor mode switching, and that exploiting mode switching improves dynamic performance.

Note that under condition (d), the approximation in (9) slightly relaxes the velocity–torque constraint in (8), which involves a max function. However, the violation of the original constraint—defined as the maximum excess ratio of the optimal torque over $\tau^{\lim}(v)$ computed by (8)—was at most 0.84%. Therefore, the effect of the constraint approximation is considered negligible.

B. *Real-Robot Experiments*

To verify that the optimized trajectory with mode switching can be executed on the real robot, we conducted real-robot experiments.

The supply voltage was set to 36 V to provide sufficient headroom for current control relative to the 24 V used to define the joint velocity constraints.

We used the following joint position controller to compute the commanded torque τ_i^{ref} for joint i from the reference joint angle and velocity, q_i^{ref} and v_i^{ref}, and the measured joint angle and velocity, q_i^{act} and v_i^{act}. Here, $K_{\mathrm{p},i}$, $K_{\mathrm{d},i}$, and τ_i^{VF} denote the proportional gain, derivative gain, and viscous-friction feedforward torque, respectively.

$$\tau_i^{\mathrm{ref}} = K_{\mathrm{p},i}(q_i^{\mathrm{ref}} - q_i^{\mathrm{act}}) + K_{\mathrm{d},i}(v_i^{\mathrm{ref}} - v_i^{\mathrm{act}}) + \tau_i^{\mathrm{VF}} \tag{14}$$

The motor voltage V_i^{out} is determined so that the actual current I_i^{act} tracks the reference current I_i^{ref} computed from the commanded torque:

$$V_i^{\mathrm{out}} = k_{\mathrm{i},i}\int (I_i^{\mathrm{ref}} - I_i^{\mathrm{act}})dt + k_{\mathrm{p},i}(I_i^{\mathrm{ref}} - I_i^{\mathrm{act}}) + V_i^{\mathrm{EMF}} \tag{15}$$

$k_{\mathrm{i},i}$ and $k_{\mathrm{p},i}$ denote the integral and proportional gains, respectively. V_i^{EMF} is a feedforward voltage that includes a back-EMF compensation term computed from the joint velocity and the back-EMF constant (the inverse of the speed constant). To keep the current-control bandwidth constant despite changes in circuit parameters due to mode switching, we scaled the integral gain, proportional gain, and back-EMF compensation term in proportion to the winding resistance, inductance, and back-EMF constant, respectively.

The recovered schedule for condition (d) is summarized in Table IV.

TABLE IV: Recovered mode schedule for condition (d). It follows A–B–C–B–A, with four switches and a minimum dwell time of 0.05 s.

Time (s)	0.00–1.34	1.34–1.40	1.40–1.57	1.57–1.62	1.62–3.00
Mode	A	B	C	B	A

Table V shows the peak forward end-effector velocity and the peak left elbow joint velocity in the real-robot experiments under the above conditions. The real-robot motion trajectory for condition (d) is shown in Fig. 7. The left elbow joint velocity for each condition is shown in Fig. 8.

TABLE V: Peak forward end-effector velocity and left elbow joint velocity in the real-robot experiments. The percentages indicate the ratios relative to the peak velocities of the optimal trajectories.

Condition	(a)	(b)	(c)	(d)
Peak forward velocity of the end-effector (m/s)	6.20 (100.0%)	7.95 (97.4%)	8.24 (99.7%)	9.01 (101.4%)
Peak left elbow joint velocity (rad/s)	-3.93 (101.6%)	-7.80 (101.9%)	-9.19 (100.7%)	-10.23 (101.6%)

In the experiments, the robot was able to execute the motion in all conditions without losing balance or falling. As in the optimal trajectories, the peak forward end-effector velocity and the peak left elbow joint velocity were highest in condition (d), where mode switching was allowed. The errors relative to the optimal trajectories were within 2.6% for the peak forward end-effector velocity and within 1.9% for the peak left elbow joint velocity, indicating sufficiently accurate tracking.

In addition, the time history of the voltage applied to the VC motor under condition (d) is shown in Fig. 9. The voltage changes discretely at each mode transition and is kept low even during high-speed motions as the mode shifts from A to B and then to C. Although the voltage exceeds the ± 24 V reference in magnitude immediately before a mode switch during acceleration in some intervals, this is attributed

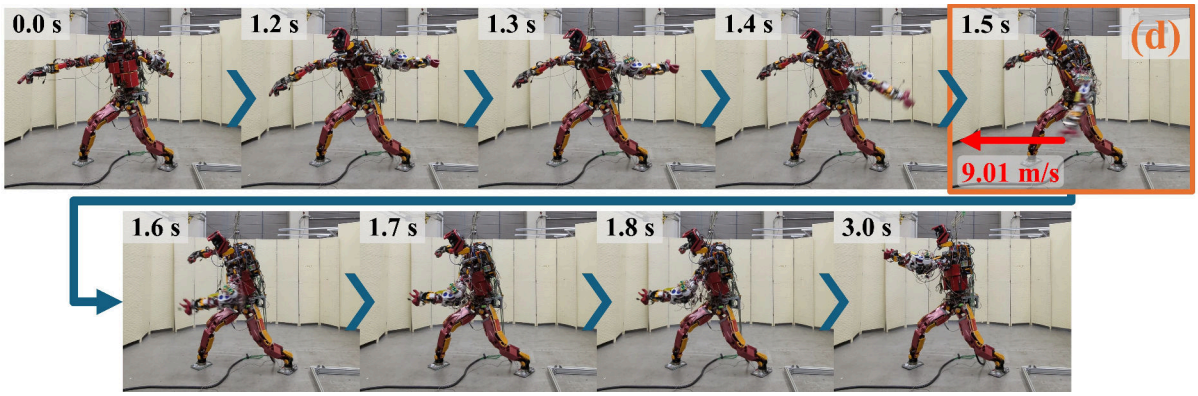


Fig. 7: Real-robot arm-swing trajectory under condition (d), where mode switching is allowed. The motion achieves a peak forward end-effector velocity of 9.01 m/s, which is the fastest among all conditions.

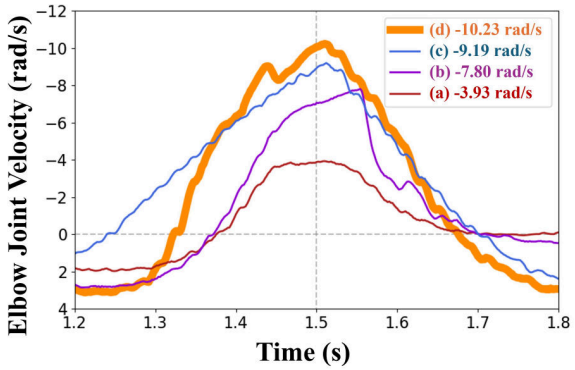


Fig. 8: Left elbow joint velocity on the real robot; condition (d) with mode switching achieves the highest peak of -10.23 rad/s.

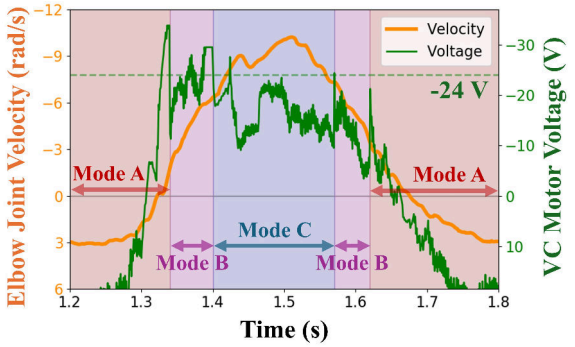


Fig. 9: Voltage applied to the VC motor in condition (d). Switching to Mode B (intermediate) and Mode C (high speed) keeps the voltage low during fast motion. For most of the motion, it remains within ± 24 V, the reference for the speed limits.

to modeling errors in the rotor inertia and viscous friction coefficient, which required a larger-than-expected current for acceleration. Nevertheless, for most of the time, the voltage remains within ± 24 V, which serves as the reference for the speed limits. These results demonstrate that the target arm-swing motion requiring both torque and speed was realized on the real system by leveraging mode switching of the VC motor.

V. Conclusion

We proposed a trajectory-optimization-based method for generating dynamic humanoid motions that exploit VC motor mode switching by imposing the union of the speed–torque ranges across multiple modes with different output characteristics as a constraint.

Using the proposed method, we computed an optimal trajectory that maximizes the forward end-effector velocity of a humanoid equipped with a VC motor at the elbow joint, and successfully generated an arm-swing motion that includes mode switching. Compared with the case where the output characteristics are fixed, the peak elbow joint velocity and peak forward end-effector velocity increased by 10.2% and 7.7%, respectively, demonstrating that variable output characteristics enhance dynamic motion performance. Furthermore, real-robot experiments demonstrated an arm-swing motion that achieves both high torque and high speed by leveraging mode switching. Although the real-robot validation in this paper uses a single VC motor at the left elbow for an arm-swing motion, the formulation itself can be applied to multiple joints with variable output characteristics.

As future work, we will incorporate speed–torque switching constraints into online motion planning to improve robustness to disturbances, including modeling uncertainties. Validation with multiple VC motors and behaviors with changing contact states, such as running and jumping, remains future work.

References

[1] H. Tada, et al. Development of Variable Chain Motor with Shape and Speed-Torque Characteristics Variability and Its Application to a Humanoid. In *2025 IEEE/RSJ International Conference on Intelligent Robots and Systems (IROS)*, pp. 21102–21109.

[2] D. Wei, et al. The concept of a jumping rescue robot with variable transmission mechanism. In *2011 IEEE International Symposium on Safety, Security, and Rescue Robotics*, pp. 99–104.

[3] A. Girard and H. H. Asada. A two-speed actuator for robotics with fast seamless gear shifting. In *2015 IEEE/RSJ International Conference on Intelligent Robots and Systems (IROS)*, pp. 4704–4711.

[4] W. Shin, et al. A Passively Adaptable Toroidal Continuously Variable Transmission Combined with Twisted String Actuator. In *2022 IEEE International Conference on Robotics and Automation (ICRA)*, pp. 11409–11415.

[5] J. Sun and C. Zhou. Advancing Robotic Jumping with CVT Enhanced SEA. In *Towards Autonomous Robotic Systems*, pp. 73–84, 2025.

[6] S. Sin, et al. Improvement of the Constant-Power Speed Range of Surface-Permanent Magnet Machine Using Winding Switching. *IEEE Access*, Vol. 9, pp. 32298–32309, 2021.

[7] Y. Notohara, et al. Winding changeover motor drive device, drive control method for winding changeover motor, and refrigeration and air-conditioning device using same. International Patent WO 2016/051456 A1, 2016.

[8] F. Copt, et al. Dynamic winding reconfiguration of a brushless DC motor. In *2017 IEEE International Electric Machines and Drives Conference (IEMDC)*, pp. 1–6.

[9] A. Girard and H. H. Asada. A practical optimal control approach for two-speed actuators. In *2016 IEEE International Conference on Robotics and Automation (ICRA)*, pp. 4572–4577.

[10] A. Girard and H. H. Asada. Leveraging Natural Load Dynamics With Variable Gear-Ratio Actuators. *IEEE Robotics and Automation Letters*, Vol. 2, No. 2, pp. 741–748, 2017.

[11] S. Sovukluk, et al. Realtime Limb Trajectory Optimization for Humanoid Running Through Centroidal Angular Momentum Dynamics. In *2025 IEEE International Conference on Robotics and Automation (ICRA)*, pp. 404–410.

[12] H. Qi, et al. A Three-Step Optimization Framework With Hybrid Models for a Humanoid Robot's Jump Motion. *IEEE Transactions on Automation Science and Engineering*, Vol. 22, pp. 14120–14132, 2025.

[13] R. Terasawa, et al. Achievement of dynamic tennis swing motion by offline motion planning and online trajectory modification based on optimization with a humanoid robot. In *2016 IEEE-RAS International Conference on Humanoid Robots (Humanoids)*, pp. 1094–1100.

[14] K. Kojima, et al. Development of life-sized high-power humanoid robot JAXON for real-world use. In *2015 IEEE-RAS 15th International Conference on Humanoid Robots (Humanoids)*, pp. 838–843.

[15] J. A. E. Andersson, et al. CasADi – A software framework for nonlinear optimization and optimal control. *Mathematical Programming Computation*, Vol. 11, No. 1, pp. 1–36, 2019.

[16] A. Wächter and L. T. Biegler. On the implementation of an interior-point filter line-search algorithm for large-scale nonlinear programming. *Mathematical Programming*, Vol. 106, No. 1, pp. 25–57, 2006.

[17] J. Carpentier, et al. The Pinocchio C++ library : A fast and flexible implementation of rigid body dynamics algorithms and their analytical derivatives. In *2019 IEEE/SICE International Symposium on System Integration (SII)*, pp. 614–619.